Research Article

Journal of Electrical Electronics Engineering

The Occurrence of Primary REE Minerals and Their Para genesis within S-Type Granite and Quartz Vein, South Bangka, Bangka Belitung Islands, Indonesia

Armin Tampubolon[1, 2]*, Ildrem Syafri[1], Mega Fatimah Rosana[1], Euis Tintin Yuningsih[1]

[1]*Faculty of Geological Engineering, Padjadjaran University, Bandung, West Java, Indonesia*

[2]*Center for Mineral Coal and Geothermal Resources, Geological Agency, Ministry of Energy and Mineral Resources*

***Corresponding author**
Armin Tampubolon, Faculty of Geological Engineering, Padjadjaran University, Bandung, West Java, Indonesia

Submitted: 23 Aug 2022; **Accepted:** 29 Aug 2022; **Published:** 26 Sep 2022

Citation: *Tampubolon A*, Syafri I, Rosana MF, Yuningsih ET. (2022). The Occurrence of Primary Ree Minerals and Their Paragenesis within S-Type Granite and Quartz Vein, South Bangka, Bangka Belitung Islands, Indonesia. J Electrical Electron Eng, 1(1),64-86.*

Abstract

Primary rare earth element (REE) minerals known as carbonate and phosphate were identified in some localities. The carbonate type consists mainly of parasite, allanite, and bastnaesite, while REE phosphate group comprises mainly monazite and xenotime. They are accompanied by thorite and zircon. REE-bearing quartz vein is associated with cassiterite, pyrite, chalcopyrite, sphalerite, and tourmaline. The hydrothermal fluid that plays a role in REE mineral precipitation is subdivided into three stages: early (> 316oC - 316oC), medium (< 316oC – 210oC), and late (<210oC-190oC). The δ18O range which is 12, 7 ‰ – 13 ‰, and the δ34S range are 3, 9 ‰ – 5, 5 ‰ indicate that the origin of hydrothermal fluid comes from mixing fluids of both meteoric and magmatic sources, and also influenced by metamorphic waters. While the source of sulphur is granitic and sedimentary rocks. REE phosphate is thought to have formed in the early magmatic crystallization stage except for monazite formed in the medium magmatic-hydrothermal and late hydrothermal stages. Primary REE carbonate may have formed in a medium hydrothermal-magmatic stage except for parasite and allanite, they may have formed in late-stage hydrothermal. Chalcopyrite and sphalerite seem to be associated with REE minerals in the medium and late hydrothermal stages.

Key Words: REE phosphate, REE carbonate, granite, hydrothermal, early stage, medium stage, late stage.

Introduction

Rare earth elements (REE) consist of 17 (seventeen) elements from the lanthanide group (La, Ce, Pr, Nd, Pm, Sm, Eu, Gd, Tb, Dy, Ho, Er, Tm, Yb, and Lu) plus Y and Sc which have similar chemical and physical properties. REE is categorized as a part of critical mineral resource due to its important uses in modern technology and the limited resources that are only dominated by one country, i.e., China [1, 2]. REEs are generally produced from two types of deposits namely primary deposits, which are associated with carbonatite, and secondary ones, which are associated with weathering products [3]. The indication of primary REE minerals related to granitic rocks has recently been reported from several countries, among which are in the Southeast Asia Tin Belt such as Myanmar, Thailand, and Laos.

In Indonesia, efforts to discover potential REE deposits at the economic level have been done for the last decade. REEs are mostly observed associated with the tin deposit as REE phosphate minerals such as monazite and xenotime. They are found within alluvial deposits and the tailing of tin mines [4-6]. However, due to the lack of research on the origin of primary REEs, it is not known where they come from. Monazite and xenotime, in general, form in the initial crystallization stage of magma; although they may form as a result of reacting with apatite crystals and dissolved fluid, hydrothermal process, and metasomatic. In granite, monazite infills pores and fractures in apatite [7]. Sometimes anhedral-subhedral xenotime crystals associate with monazite. Meanwhile, REE mineral grains distributed as monazites are largely found by local people from the tailing of tin mines, which they collect together with cassiterite and other mineral commodities.

The indication for primary REE minerals, in this context, is defined as REE minerals formed during magmatic crystallization, and post-magmatic hydrothermal processes. The primary indication was observed in veinlets within biotite granite that have been altered to quartz, apatite, zircon, and pyrite [8]. In addition, it was also discovered within quartz veins in weathered granite bodies at Jangkang and Pulau Tinggi, Sungai Liat, North Bangka. From the measurement of fluid inclusions, it shows that tin was formed at low temperatures (210-220o C) with a salinity of 5-6 wt. % NaCl

eq. [9]. In general, the temperature of the hydrothermal fluid in depositing cassiterite ranges from 250 to 450oC [10]. This means that the range of temperature formation for cassiterite in the Bangka Belitung is within the interval of 210 oC and 450 oC. Based on previous investigation results, granite in South Bangka has significant REE values. Granite identified as biotite granite has REE content of 297.53 ppm in Toboali, 302.34-316.59 ppm in Pading (Simpang Rimba), and 274.08 ppm in Permisan [11].

This paper attempts to expose and discuss the origin of primary REE minerals within both granite and quartz vein in South Bangka, Bangka Belitung, Indonesia. The focused areas are located in Toboali and Air Gegas. Selected laboratory methodologies were performed to obtain the content of REE primary minerals and parameters for the interpretation of their par agenesis.

Geology

The research area is part of the Southeast Asian tin belt in Bangka Island, one of the excellent tin producing areas. It is largely covered by granite rock known as Triassic-Jurassic Kelabat Granite. This rock consisting of I-type and S-type granites intruded the Permo-Carbon Pemali Complex in the form of phyllites, schists, and gneiss of Permo-Carbon age and the Triassic Tanjung Genting Formation which is composed of alternating metasedimentary claystone, siltstones, and sandstones of Triassic age [12, 13]. The Kelabat granite from the Late Permian to Late Triassic occupies West, South, Central, and East Bangka. The lithology of this granite consists of granite, granodiorite, Adam elite, diorite, and S-type and I-type quartz diorite [14].

The Southeast Asian tin belt itself consists of three granite provinces, namely, the East Belt with a north south trend is dominated by I-type granite, the Main Belt across Thailand, Malaysia, and Indonesia is occupied by S-type granite while the West Belt across Thailand and Burma represented by S-type granite and I- type granite . The N–S Paleo-Tethys Bentong-Raub suture line that divides peninsular Malaysia into the Sibumasu Block in the west and the Indochina Block in the east also crosses the eastern part of Bangka Island in the Bangka-Belitung Sea but is not exposed on land [15].

Tin mineralization is grouped according to the location of the granite pluton, divided into two types: Main Range including S-type Kelabat Granite, and I-type Eastern Belt granite. Sn-W ores come from the Main Pluton (Figure 1) [16, 17]. In placer tin deposits, REE occurs as monazite, xenotime, and zircon minerals. It is interpreted that REEs are derived from Kelabat Granite rocks as found in South Bangka [18, 19].

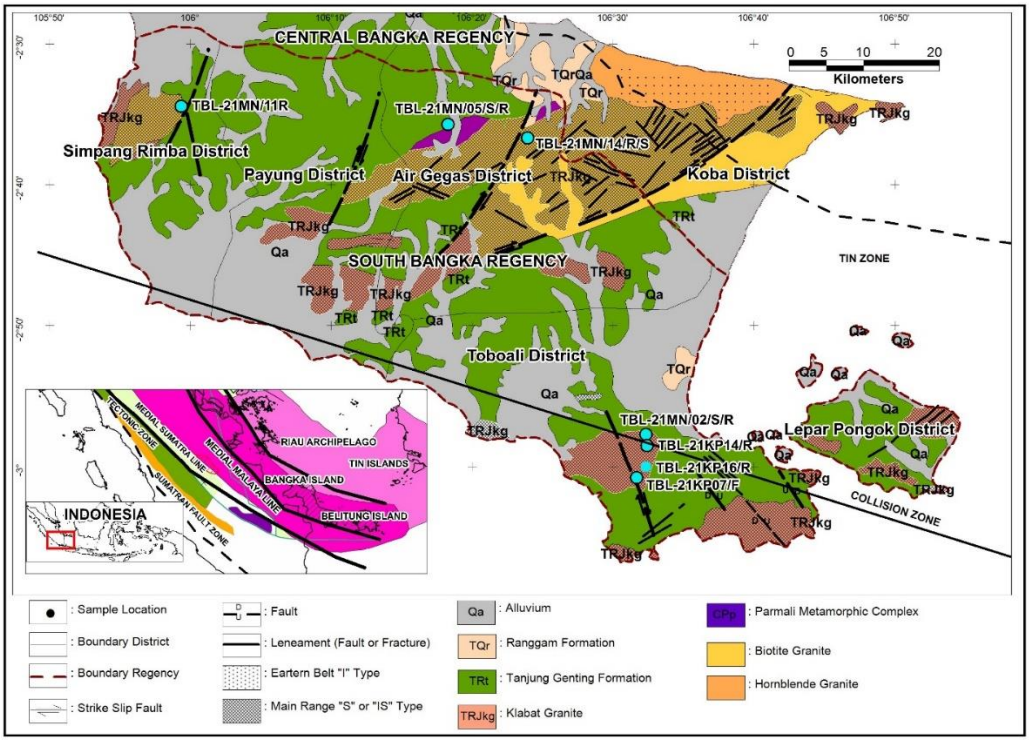

Figure 1: Geology of the South Bangka and Locations of Rock Sampling

Granite Observation and Sampling

Six samples were collected from the base of weathering profiles: three from Toboali (TBL-21MN/02B/R, TBL21KP16/R, TBL21KP-7/F), and two from Air Gegas (TBL-21MN/05E/R, TBL-21MN14/R), and one from Simpang Rimba (TBL-21MN/11/R). Photos of samples TBL-21MN/02B/R, 21MN/05E/R, and TBL-21MN14/R are shown in Figures 2, 3, and 4 respectively [20, 21]. Two samples (TBL 21 KP/ 07/F dan TBL-21KP/16/F), Toboali, are a relatively fresh granite rock, they are gray in color, aphanitic texture and contain quartz, feldspar, and iron oxide, presumably the bottom part of the alluvial weathering profile. On the basis of the geological map of a 1:250,000 scale, the sample numbers TBL-21MN/05E/R and TBL-21MN/14/R, Air Gegas, are within the contact between the Pemali Complex and the Kelabat Granite (Figure 1), samples were collected from the bottom of the pit The indication of strong deformation is found in Toboali granite marked with a lateral fault in the north along with NW-SE foliation. The granitic plutons identified at Toboali and Simpang Rimba are composed of hornblende and biotite as mafic minerals. The Toboali and Simpang Rimba Plutons are classified into young magmatic episodes. The plutons have an average magmatic age of 220 million years. In general, the granite observed in Toboali and Air Gegas has a medium texture, composed of quartz, feldspar, and biotite ± hornblende. Quartz veins are discovered within granite in the bottom of the weathering profile at the Air Gegas mine (TBL-21MN/5E/R). So far, no fresh granite has been observed at the bottom of the Air Gegas tin mine as it is submerged in the water.

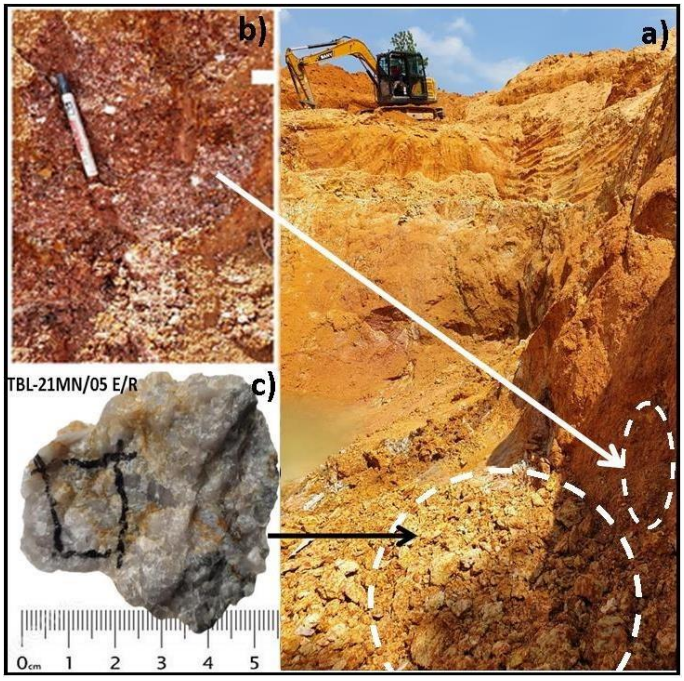

Figure 3: (a). Sampling location TBL-21MN/05E/R at Air Gegas tin, mine pit, 20 m depth. (b). Relics of feldspar, biotite and quartz within weathered granite. (c). the quartz vein hosted in the granite, showing the weathering of cream-colored feldspar and cloudy white quartz, containing metallic sulphides and cassiterite

Figure 4: Sample location of TBL-21MN/14/R. a) Laterite profile in the granite, Air Gegas Area. b) Quartz vein of 5 cm thick in the weathered granite (position N 300 E/60). c) Vein with quartz (white) and tourmaline (black).

Analytical Methods

X-Ray Fluorescence analyser (XRF) and Inductively Coupled Plasma Mass Spectrometry and Optical Omission (ICP- MS) analyses were conducted at Intertek Laboratory Jakarta, Indonesia. They applied ICPMS and OES) Determination 4 acid digest in Teflon tube for REE and trace elements besides ICP-OES Determination 4 acid digest in Teflon tube. Samples were dried and crushed by a jaw crusher or iron mortar and were ground by a mill. Major and trace elements including REE were determined using XRF and ICPMS Agilent type 7700 and ICP-OES Agilent type 725. Solution of rock samples for ICP-MS analyses was made
By acid digestion of fused glass bead using lithium meteorite and tetra borate as flux.

Petrographic descriptions and ore microscopy were carried out at the Laboratory of the Centre for Mineral Coal and Geothermal Resources, Geological Agency of Indonesia. X-Ray Diffraction (XRD) was performed at the Laboratory of Centre for Geological Survey, Geological Agency of Indonesia, and Laboratory Wuhan Centre, China Geological Survey (CGS). The main XRD instrument used is Analytical X'Pert PRO with type series of PW3040/x0 X'Pert PRO, made in Nederland [22, 23]. For the test of sample materials totally, they used Cu-tube with a spinning sample holder or flat sample holder. The measurement angle (2theta) that is used to perform was around 30 – 600. Grinding tools used were agate grinders with grain sizes ranging 5 – 10 um or approximately 200 mesh.

SEM-EDX/EDS instruments applied for analysis were of type JEOL JED-2200 Series (SEM JEOLJSM6360LA). This work was performed at the Laboratory of the Centre for Geological Survey, Geological Agency of Indonesia in Bandung. The chemical compositions of minerals were measured using a Shimadzu EPMA 1600 at the laboratory of Wuhan Centre, CGS, and China. At the same time, backscattered electron (BSE) images were also taken. During quantitative analysis, the operating conditions were set as follows: 15 kV accelerating voltage, 10 nA beam current, and 1 µm beam diameter. Minerals from SPI company of America were used as standards, and a program based on the ZAF procedure was used for data correction.

To obtain the secondary image of BSE and their REE composition, further methods were performed. A JEOL JSM_7500F- SEM coupled with Oxford Aztec X-MaxN Energy Dispersive Spectroscopy (EDS) analyzed the element composition of REE-bearing minerals. These minerals were tested in the setting of 15kV accelerating voltage, 10μA beam current, and 6.5-8mm work distance [24, 25]. Scanning electron microscopes equipped with an X-ray energy spectrometer achieve the mapping of the high-resolution elements to obtain the chemical compositions of small areas of samples.

Fluid inclusion studies were conducted at the Wuhan Center Laboratory, China Geological Survey, China. Two samples were selected, namely: TBL-21MN/05E/R, and TBL-21MN/14/R, both samples are of transparent quartz veins. Such samples were first checked to see if they were rich in fluid inclusions, afterward a 0.3 mm thin section thick was made. Measurements were performed using the AXiolab polarizing microscope and the LINKAM THMS heating–freezing stage according to the EJ/T 1105-1999 standard. Parameters measured were homogenization temperature (Th), final ice melting temperature (Tm), and determination of salinity (w% NaCl eq). Individual fluid inclusion composition was measured using the RENISHAEW Raman Spectrometer and Leica Deflected Microscope.

Stable isotopes O and S were carried out at the Wuhan Center Laboratory, China Geological Survey, and China. The analytical method of quartz grains is separated using a binocular microscope to ensure 99% purity. Quartz is reacted with BrF5 to release oxygen at 550°C, impurities are removed by freezing, purified O2 is converted to CO2 by reacting with graphite at 700°C, and collected by freezing. The oxygen isotope composition was determined using the MAT-253 mass spectrometer [26, 27]. The results are reported in conventional notation relative to the Vienna standard mean ocean water (V-SMOW). Analytical accuracy ± 0.2‰. The stable isotope S analysis was also carried out at the Wuhan Center Laboratory, China Geological Survey, and China. Fresh ore samples are ground to a size of 40-80 mesh. Single sulfide granules were taken from samples ground under a binocular microscope, with a purity of more than 99%. Sulfur isotope analysis was performed using MAT-251. The 34S/32S ratio is expressed as 34S per mil value relative to the standard Vienna Cannon Diablo Troilite (V-CDT) to an accuracy of 0.2‰

Results

Petrography Description of Granitic Rocks

Four samples were observed under petrography, namely samples TBL-21MN/2B/R, TBL21 KP-14/R from Toboali, TBL-21MN/5E/R, and TBL 21MN/14/R from Air Gegas. Sample TBL-21MN/2B/R shows colorless, holocrystalline, hypidiomorphic granular, fine grain size up to 8.0 mm, euhedral to anhedral crystals, consisting of quartz (35%), orthoclase (30%), plagioclase (5%), microcline (12%), hornblende (6 %), biotite (4%), clay (3%), monazite (1%), zircon (1%), chlorite (1%) and opaque minerals (2%) (Figures 5 A and B). Sample TBL-21MN/5E/R shows colourless, holocrystalline, hypidiomorphic granular, fine grain size up to 6.0 mm, subhedral-euhedral crystals, composed of quartz (50 %), orthoclase (17 %), monazite (20 %), cassiterite (12 %), opaque minerals (1 %) (Figures 5C and 5D). Sample TBL21 KP-14/R shows holocrystalline, hypidiomorphic granular, size up to 3 mm, euhedral-anhedral crystals, composed of quartz (60 %), orthoclase (26 %), muscovite (5 %), plagioclase (4 %), chlorite (3 %), and opaque minerals (2 %) (Figures 5 E and F). Sample TBL 21MN/14/R has textures: holocrystalline, hypidiomorphic granular, grain size up to 4 mm, composed of quartz (> 90%), cassiterite (5%), pyroxene (1%), and opaque (1%) (Figures 5 G and H).

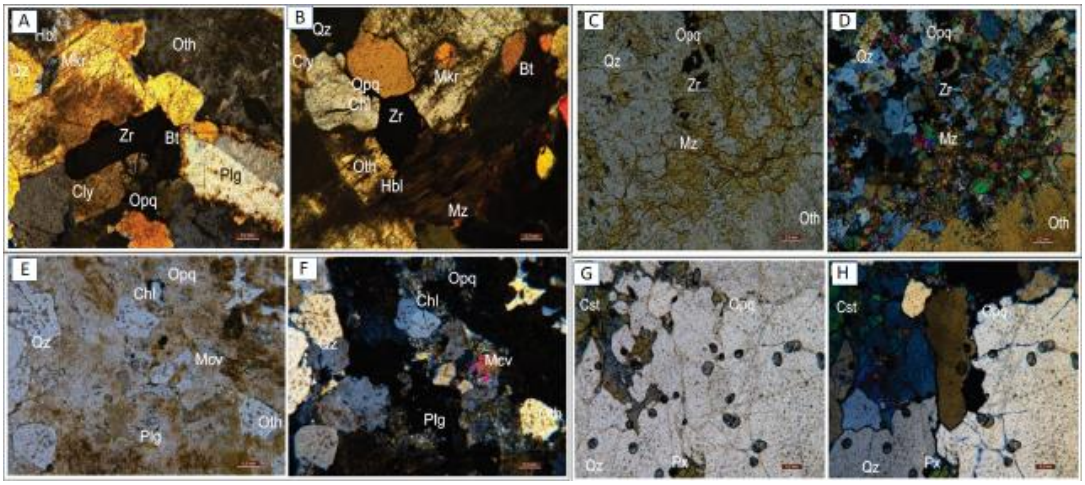

Figure 5: Photomicrograph of sample TBL-21MN/02BR on cross nicol (A and B), Toboali, consist of orthoclase (Oth), biotite (Bt), plagioclase (Plg), hornblende (Hbl), microcline (Mkr), clay (Cly), zircon (Zr), and opaque (Opq) (A), in addition, quartz (Qz) and monazite (Mz) (B). Sample TBL-21MN/5E/R (parallel nicol C and cross nicol D), Air Gegas, consist of quartz (Qz), microcline (Mkr), zircon (Zr), and opague (Opq) (C, parallel nicol), in addition, orthoclase (Oth), and monazite (Mz) (D). Sample TBL21 KP-14/R Toboali (E, parallel nicol, and F, cross nicol) consisting of quartz (Qz), orthoclase (Oth), muscovite (Msv), chlorite (Chl),

plagioclase (Plg), and opaque (Opq). Micrograph of sample TBL 21MN/14/R (G, parallel nicol, and H, cross nicol) Air Gegas, consisting mainly of quartz (Qz), cassiterite (Cst), pyroxene (Px), and opaque (Opq). Magnification 50x

Ore Microscopy

Three samples were observed on the polish section using reflected polarization microscopy: samples TBL21MN/02B/R Toboali, TBL-21MN/05E/R, and TBL-21MN/14/R Air Gegas. Under the microscope, sample TBL-21MN/02B/R that was taken from the bottom of the lateritic profile, are observed to contain pyrite, chalcopyrite < 0.5 %, stannite (Cu2FeSnS4) < 0.5 %, magnetite (trace), and sphalerite (trace) (Figure 6). It is shown that stannite and chalcopyrite are in intergrowth with each other. Cassiterite (SnO2) was clearly observed on a polished section of sample TBL-21MN/05E/R (quartz vein), Air Gegas (Figure 7). Ore minerals such as cassiterite (SnO2), hematite (Fe2O3), and hydrous iron oxide were also observed on a polished section of sample TBL-21M/14/R, Air Gegas (Figure 8).

Figure 6: Photomicrograph of polished section sample TBL-21MN/02B/R consisting of pyrite (Py) 2%, kalkopirit (Cp) < 0,5%, stannite (Stn) < 0,5%, magnetite (Mgt) (trace), and sphalerite (Sp) (trace). Mag. 50x

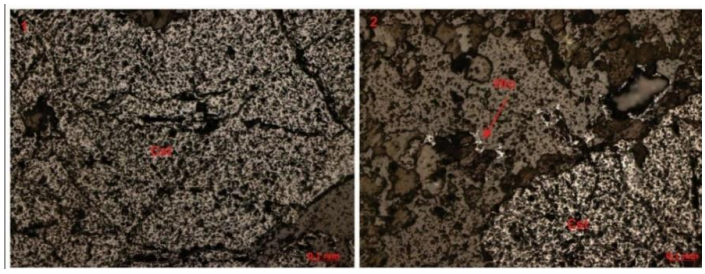

Figure 7: Photomicrograph of polished section sample TBL-21MN/05E/R Air Gegas, composed of cassiterite (Cst) 20% and hydrous iron oxide 3%. Mag. 50x

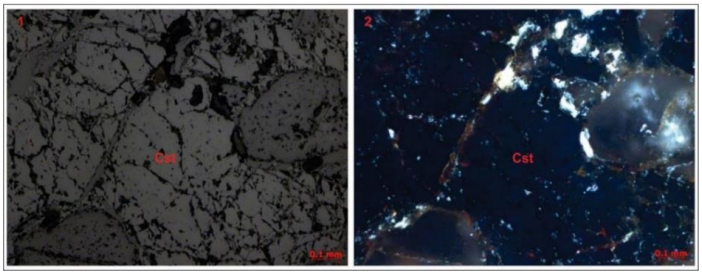

Figure 8: Photomicrograph of the polished section of the granite sample TBL-21MN/14/R Air Gegas nicol cross (1) shows the colour of reflection in cassiterite (Cst) and appears to have holes and cracks in the rock mass (2). Contains ore minerals cassiterite (25 %), hematite (trace), and hydrous iron oxide (1 %). Mag. 50x

Major/trace elements, and REE

Nine samples of granites were analysed for major and trace elements using the XRF method, the analysis results are shown in Table 1. The silica content of granite samples ranges from 72.4% to 76.17%, and the highest quartz content, which is more than 84%, is shown in the granite that hosts quartz veins (TBL21MN/5E/R). Using Middlemost diagram plots (1994), most rock samples are classified into granite (Figure 9a) where their magmatic sources are grouped into high K-alkaline or calc-alkaline series (Figure 9b), and the chemical composition of magma fluid is per aluminous (Figure 9c). Using the Rb versus (Y + Nb) diagram can be shown that the granite is emplaced in syncollisional and within-plate tectonic settings (Figure 9d). The REE pattern of the granite tends to be enriched from heavy rare earth elements (HREE) toward light rare earth elements (LREE) with a sharply negative anomaly for Eu (Figure 10a). Total REE content ranges from 180.80 ppm to 1126.6 ppm, where the highest value belongs to sample TBL-21MN/02B/R from Toboali. Sample TBL-21KP/07/R has the second-highest REE value, which is 1014.69 ppm. The LREE values are much higher than the HREE values [28-30]. A primitive mantle-normalized spider diagram (McDonough & Sun, 1995) shows the enrichment of large-ion lithophyte elements (LILEs) in granite, such as Pb, Rb, Cs, and K, exhibiting negative anomalies for high-field-strength elements (HFSEs), such as Nb, P, Zr, Ti, and negative anomalies of Ba and Sr relative to Rb (Figure 10b).

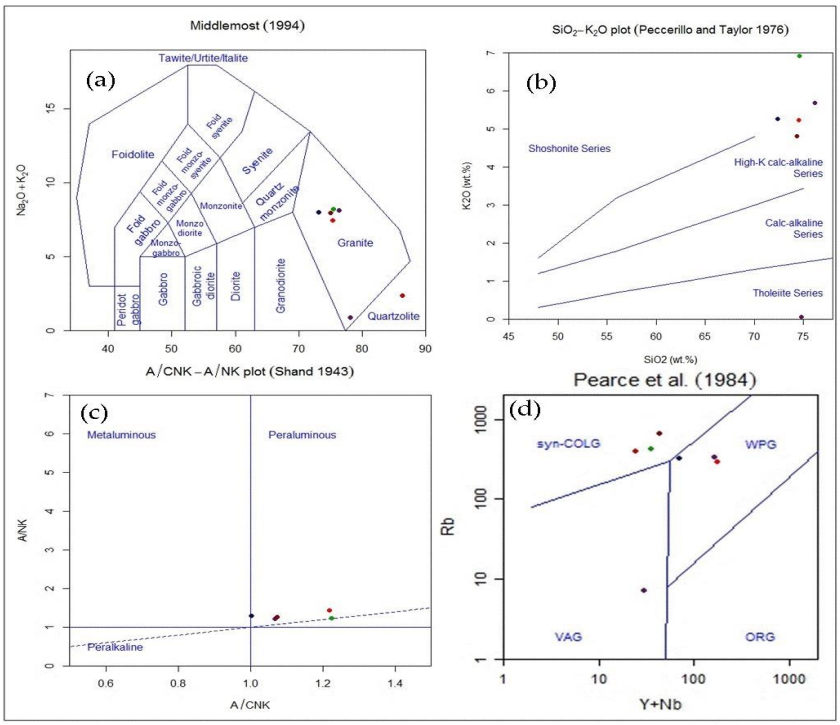

Figure 9: Major elements data of granitic rocks from Toboali and Air Gegas, South Bangka. (a). Plotting the SiO2 versus Na2O + K2O binary diagram, most of the samples are in granite areas. (b). K2O versus SiO2 wt.% using Paccerilo & Taylor diagram (1976); (c). Alumina saturation index diagram: The A/CNK (molar Al2O3/(CaO + Na2O + K2O)) ratio is greater than 1.1, and the granite is categorized as per aluminous and S-type ; (d). Y + Nb versus Rb diagram showing the tectonic setting (Pearce et al., 1984) of the South Bangka granitic rocks. Syn-COLG = syncollisional granites; VAG = volcanic-arc granites; WPG = within-plate granites; ORG = oceanic ridge granites

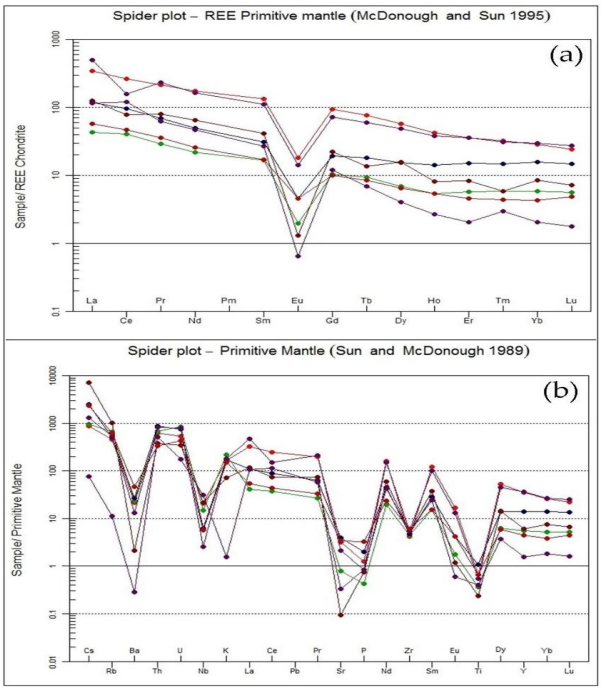

Figure 10: Chondrite normalized rare earth elements (REE) diagram (a) and primitive mantle normalized Trace element diagram (b) Normalized multi trace element values for Bangka Selatan granites (Sun & Mc Donough, 1989).

Table 1: Major/trace elements, and REE values of granitic samples from South Bangka

Sample	TBL-21MN 02B/R	TBL 21 KP 14/R	TBL 21 KP 16/R	TBL 21 KP 07/F	TBL-21MN/05 E/R	TBL-21 MN 14/R	TBL-21 MN 11/R
Major oxide element (wt%)							
SiO_2	74.53	74.57	72.4	76.17	84.79	74.81	74.3
TiO_2	0.16	0.09	0.24	0.12	0.07	0.1	0.16
Al_2O_3	13.21	11.67	13.02	12.28	7.63	11.89	13.03
Fe_2O_3	2.48	4.02	3.23	2.22	3.12	7.88	2.32
MnO	0.02	0.18	0.04	0.04	0.09	0.09	0.06
MgO	0.23	0.1	0.44	0.13	0.5	0.12	0.2
CaO	0.89	0.04	1.61	0.75	0.02	0.04	1.02
Na_2O	2.16	1.2	2.65	2.42	0.13	0.79	3.08
K_2O	5.24	6.92	5.26	5.69	2.18	0.06	4.82
P_2O_5	0.035	0.019	0.047	0.026	0.024	0.026	0.072
LOI	1.28	0.01	0.74	0.56	0.85	0.62	0.45
Total	110.24	99.82	99.68	100.41	99.04	96.43	99.51
Trace element (ppm)							
Cu	5	7	18	12	742	4	<1
Zn	102	251	38	28	60	97	31
Pb	41	104	24	60	53	13	44
Rb	289	424	320	335	660	7.2	394
Sr	66.2	16.7	84.3	45	2	7	71
Ba	151	163	189	93	15	2	323
Y	163	25.5	64.7	165	27.7	7.1	20.2
Zr	47.1	50.8	52.7	62.1	60.6	61.4	67.4
Nb	14.7	11.9	17	15	15.3	4.9	1.34
Th	52.9	58.9	75.4	70.3	32.5	44.1	28.7
U	11.4	17.8	15.6	16.8	7.28	3.7	9.13
Sb	0.3	5.4	0.5	0.7	5	0.7	0.3
Sn	2.6	10.7	4.5	1.8	142	22.5	4.1
W	<0.1	6.6	2.6	1.4	288	1.7	8.1
K	41800	54800	42300	45500	17800	390	38200
Rare earth element (ppm)							
La	222	28	77.2	322	80.9	74.5	37.5
Ce	437	67.8	160	266	131	201	78.8
Pr	54.6	7.35	17.5	58.6	20.4	15.8	9.04
Nd	220	27	61.6	204	80.6	58.1	31.9
Sm	53.7	6.8	12.5	45.2	16.7	10.8	6.9
Eu	2.8	0.3	0.7	2.2	0.2	0.1	0.7
LREE	990.1	137.25	329.5	898	329.8	360.3	164.84
Gd	51.3	5.6	10.4	39.3	12.2	6.5	5.4
Td	7.65	0.93	1.79	5.92	1.35	0.68	0.83
Dy	39	4.6	10.4	32.9	10.6	2.7	4.4
HO	6.3	0.8	2.1	5.7	1.2	0.4	0.8

Er	15.7	2.5	6.6	15.8	3.6	0.9	2
Tm	2.2	0.4	1	2.1	0.4	0.2	0.3
Yb	12.7	2.6	6.9	13.1	3.7	0.9	1.9
Lu	1.65	0.38	1.01	1.87	0.49	0.12	0.33
HREE	136.5	17.81	40.2	116.69	33.54	12.4	15.96
Total REE	1126.6	155.06	369.7	1014.69	363.34	372.7	180.8

EPMA Analysis Dan BSE Images

Based on the results of the EPMA analysis of two samples, namely TBL-21MN/02B/R (granite rock) from Toboali and TBL-21MN/05E/R (quartz vein) from Air Gegas, several types of REE minerals and those containing REE have been identified, consisting of parisite, allanite, monazite, and thorite along with cassiterite (Table 2). From the BSE images, some other REE minerals were also confirmed such as bastnaesite, xenotime, and zircon that proved to contain REE as analyzed using EPMA (Table 3 and 4).

Table 2: Chemical composition of EPMA samples TBL-21MN/02B/R and TBL-21MN/05E/R

Area	**South Bangka**					
	Toboali					
Element	TBL 21MN/02 B/R (Th-1)	TBL 21MN/02 B/R (Th-2)	TBL 21MN/02 B/R (aln-1)	TBL 21MN/02 B/R (aln-2)	TBL 21MN/02 B/R (aln-3)	TBL 21MN/02 B/R- FCe-1
F	1,30	5,10	0,00	0,00	0,00	7,65
Al_2O_3	0,57	0,30	14,87	15,08	15,51	10,04
SiO_2	14,61	2,59	36,06	38,44	36,30	14,16
P_2O_5	0,00	0,00	0,07	0,08	0,08	0,00
CaO	1,22	1,56	8,87	8,91	10,01	1,99
TiO_2	0,00	0,00	1,95	1,76	2,10	0,00
FeO	2,94	0,82	11,30	13,57	14,59	4,73
Y_2O_3	1,06	1,07	0,00	0,00	0,00	4,18
La_2O_3	0,03	0,11	6,45	6,34	7,72	9,92
Ce_2O_3	0,08	0,29	10,50	9,93	11,13	16,13
Pr_2O_3	0,00	0,00	0,00	0,00	0,00	0,00
Nd_2O_3	0,18	0,09	3,78	3,37	2,98	6,51
Gd_2O_3	0,15	0,13	1,70	1,81	1,60	3,45
Ho_2O_3	0,00	0,00	0,00	0,00	0,00	0,00
ThO_2	59,28	79,58	1,66	1,64	1,18	0,01
SnO_2	-	-	-	-	-	-
Total	81,403	91,631	97,192	100,921	103,173	78,76
Mineral	Thorite		Allanite			Parisite
Area	**South Bangka**					
	Air Gegas					
Element	TBL 21 MN/05 E/R (FCe-1	TBL 21 MN/05 E/R (FCe-2)	TBL 21 MN/05 E/R (FCe-3)	TBL 21 MN/05 E/R (Th-1)	TBL 21 MN/05 E/R (mon-1)	R TBL 21 MN/05 E/R (mon-2)
F	6.93	7.30	6.42	0.00	0.00	0.00
Al_2O_3	1.34	0.00	0.00	0.00	0.00	0.00
SiO_2	13.51	8.10	2.64	7.38	0.40	3.61
P_2O_5	0.00	0.00	0.00	0.39	28.35	26.81
CaO	3.14	6.30	3.23	1.39	0.22	0.95
TiO_2	0.00	0.00	0.00	0.00	0.01	0.07

FeO	0.00	4.20	0.00	0.70	0.00	0.45
Y_2O_3	15.16	9.70	5.41	0.89	0.98	2.05
La_2O_3	0.00	9.10	16.06	0.40	18.25	15.43
Ce_2O_3	15.30	14.80	25.48	0.95	29.52	26.77
Pr_2O_3	0.00	1.68	3.00	0.06	2.65	2.95
Nd_2O_3	10.73	9.28	12.66	0.43	12.81	11.77
Gd_2O_3	4.79	4.39	5.62	033	4.65	4.55
Ho_2O_3	0.00	1.43	0.83	0.0	0.73	0.65
ThO_2	0.00	0.00	0.00	75.04	2.86	4.95
SnO_2	-	-	-	-	-	-
Total	70.907	76.255	81.347	87.964	101.43	100.994
Mineral	Parisite			Thority	Monzite	

Allanite

Allanite with chemical formula A2M3Si3O12 (OH), where A2 = Ca, Sr, and REE (Ce, La, Nd or Y) are depicted in the biotite that makes up the granite sample TBL 21 KP-07/F, Toboali. The presence of longitudinal allanite filling in the biotite cleavage and in the form of granules growing and crystallizing together with the biotite indicates primary formation (Figure 12a). Such allanite grain is more clearly seen in the secondary BSE image (Figure 12b) and contains Y, La, Ce, and Nd (Figure 12c). The content of REE oxide compounds based on confirmation of EPMA analysis shows significant values of REE (Table 3). From another view, allanite with zircon appears as inclusions in biotite (Figure 13).

Table 3: Chemical composition results measured by EPMA on sample TBL21 KP-07/F (spot KP 9- REE-1 and KP 9-REE-2), Toboali, and TBL-21MN/14/R Air Gegas

Chemical compounds	(KP7-REE-2) TBL-21 KP 07/F	(KP9-REE-1) TBL-21 KP 07/F	(KP9-REE-1) TBL-21 KP 07/F	(MN-3-REE-1) TBL-21 MN14/R
Al_2O_3	13.47	0	0	0
SiO_2	30.95	12.28	36.43	6.78
P_2O_5	0.00	0.43	0.03	18.49
K_2O	0	0.03	0.61	0.46
CaO	8.58	2.86	3.13	0.29
FeO	15.10	20.55	18.86	0
Y2O3	0	3.49	0.51	0
La_2O_3	5.56	8.76	2.30	5.49
Ce_2O_3	10.25	10.14	4.84	17.42
Pr_2O_3	1.49	2.35	0.75	0
Nd_2O_3	2.83	6.35	2.35	7.96
Gd_2O_3	1.76	2.23	0.79	2.69
Tb_2O_3	0	0	0	0
Dy_2O_3	0	0	0	0
Ho_2O_3	0	0	0	0
Er_2O_3	0	0	0	0
Yb_2O_3	0	0	0	0
Lu_2O_3	0	0	0	0
ThO_2	0.30	1.12	0.28	4.42
TOTAL	90.30	70.58	70.87	63.99
Mineral	Allanite	Allanite		Monazite

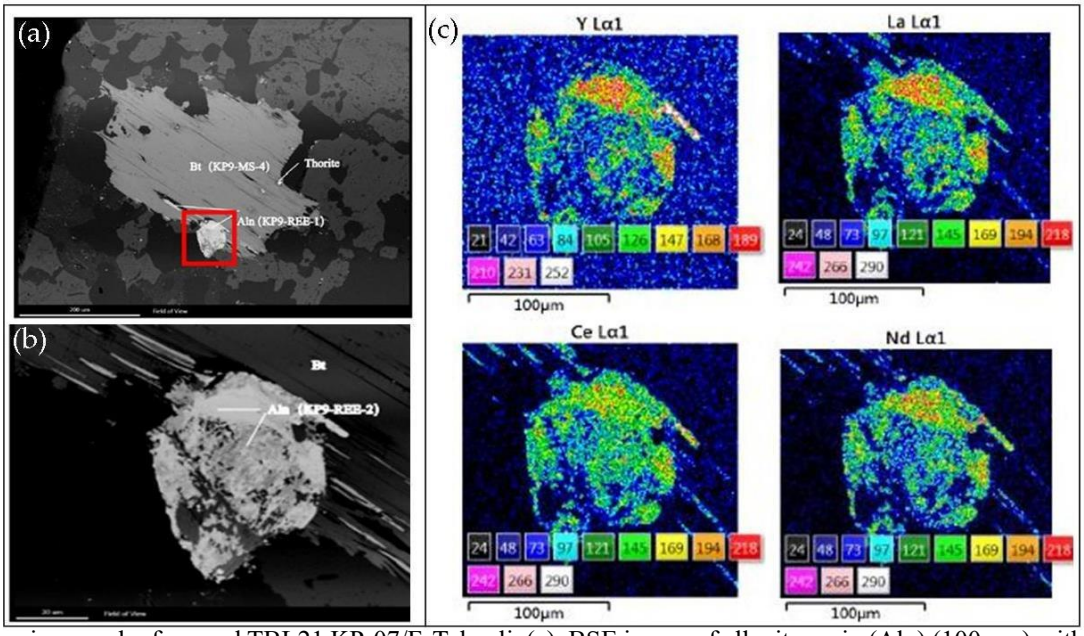

Figure 12: Photomicrograph of sampel TBL21 KP-07/F, Toboali. (a). BSE image of allanite grain (Aln) (100 µm) with thorite inclusion (< 10 µm) in biotite (Bt). (b). Secondary electron image of REE-bearing mineral (allanite). (c). REEs compositional SEM of allanite

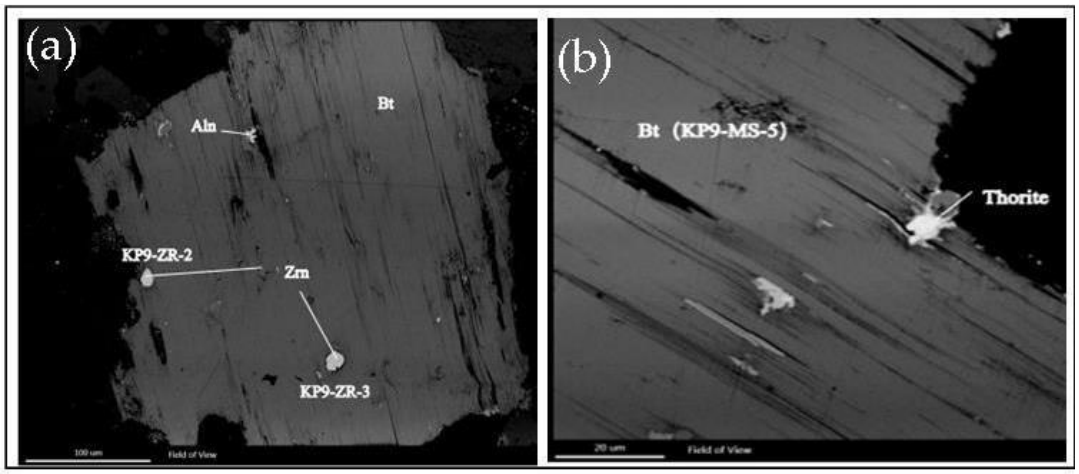

Figure 13: BSE images of a granite sample of TBL21 KP-07/F (spot KP-9-7), Toboali. (a). Allanite (Aln) with 20 µm size, overgrowth with biotite (Bt) along with zircon inclusions (Zrn) with 25 µm size (b). BSE images of sample TBL-21KP 07/F containing thorite with 25 µm size

Parasite

REE mineral of parasite ((Ca (Ce, La) 2 (CO3)3F2)) in the plagioclase and biotite are detected within the granite sample TBL-21MN/02B/R, Toboali. The elongated form of the parasite fills in the plagioclase fractures (Figure 11b) and biotite (Figures. 11e and 11f) along with inclusions of monazite, thorite, and zircon indicating the primary origin of the post-mineralized formation of monazite, thorite, zircon, and chalcopyrite in biotite (Figure 11f). The granite sample hosting mineralized quartz veins (TBL-21MN/05E)/R) is seen to have parasite that fills the biotite cleavage (Figures 15a and 15b), while the quartz vein itself is observed to contain cassiterite (Figure 15c). Secondary BSE images of parasite are depicted to contain Y, Nd, Ce, and La (Figure 14b).

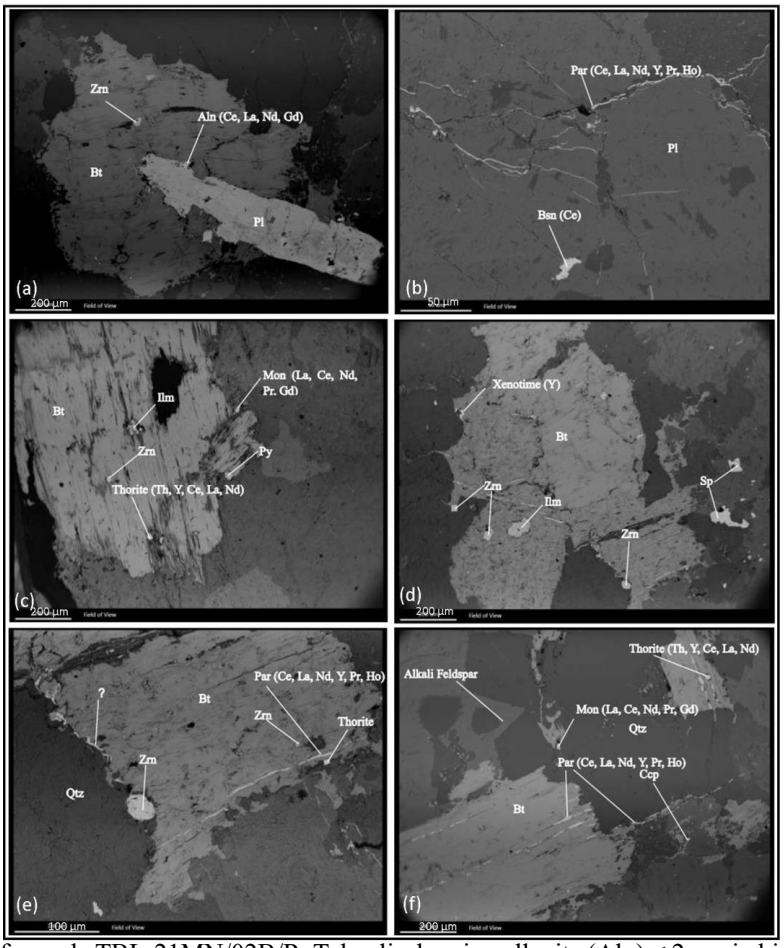

Figure 11: BSE images of sample TBL-21MN/02B/R, Toboali, showing allanite (Aln) < 2 µm in biotite (Bt) (a), parisite (Par) filling the fracture, bastnaesite (Bsn) (40 µm) in plagioclase (Pl) (b), thorite and monazite (Mon) inclusions (< 2 µm) in biotite (c), xenotime and zircon inclusions (< 2 µm) in biotite (d), parisite inclusions, zircon (50 µm), and thorite (< 2 µm) in biotite (e), inclusions of monazite and thorite (< 2 µm) and parisite filling in the cleavage of biotite (f). In addition, chalcopyrite (Ccp), sphalerite (Sp) and ilmenite (Ilm) were also seen in biotite

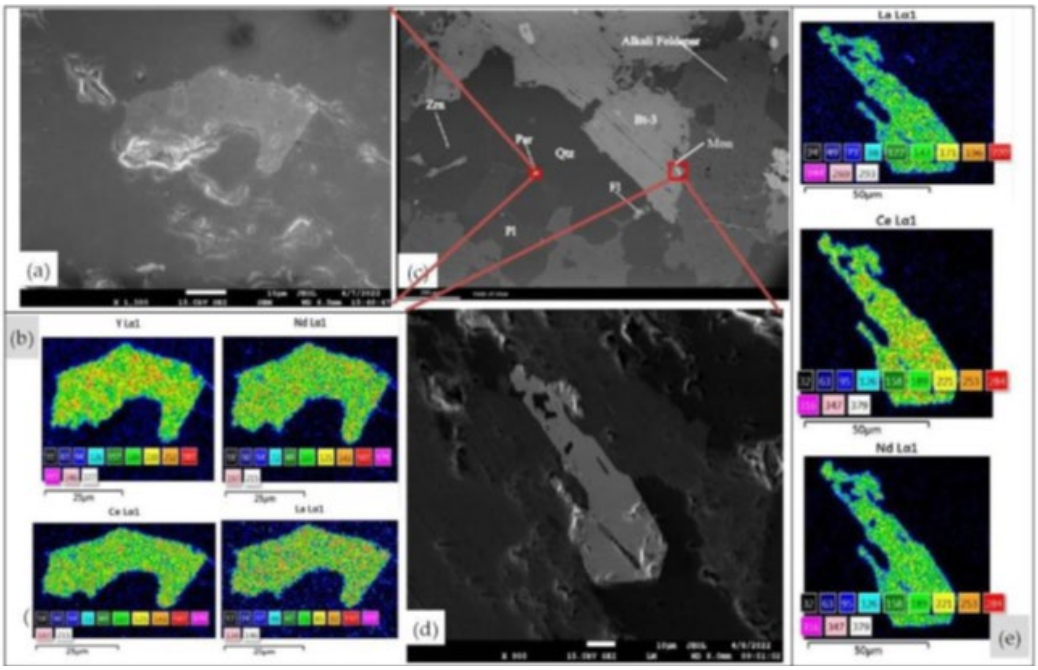

Figure 14: BSE images of sample TBL-21MN/02B/R, Toboali. (a) Secondary electron image of parasites (Par). (b). SEM compositional map of parasite. (c). Fine inclusions of the parasites, zircon and fluorite (Fl) in quartz and monazite in biotite (d) Secondary electron image of monazite. (e). SEM compositional map of monazite

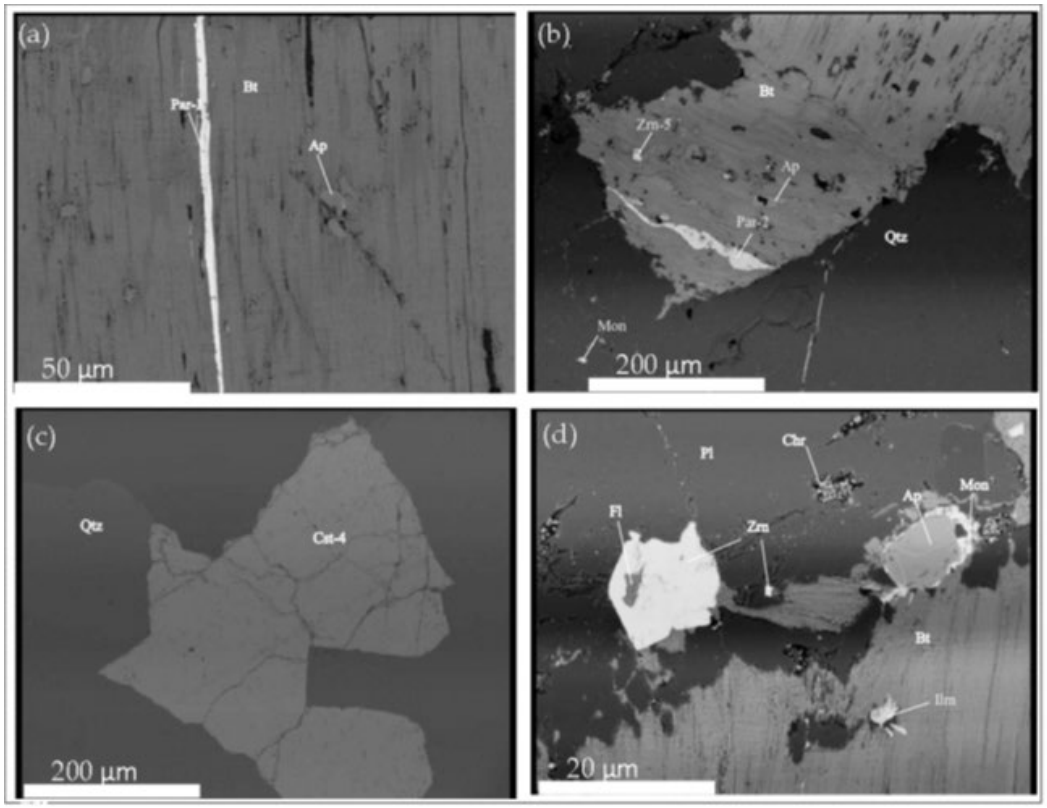

Figure 15: BSE images of sample TBL-21MN/05E/R, (a). Parisite (Par-1) filling in cleavage of biotite (Bt) and apatite inclusion. (b). Parisite filling in cleavage of biotite, along with zircon and apatite inclusions in biotite, and monazite (Mon) inclusion (10 µm) in quartz vein. (c). Cassiterite (>600 µm) in quartz vein. (d). Apatite (Ap) rimmed by monazite, chromite (Chr), zircon (Zrn) replaced by fluorite (Fl) in Plagioclase (Pl)

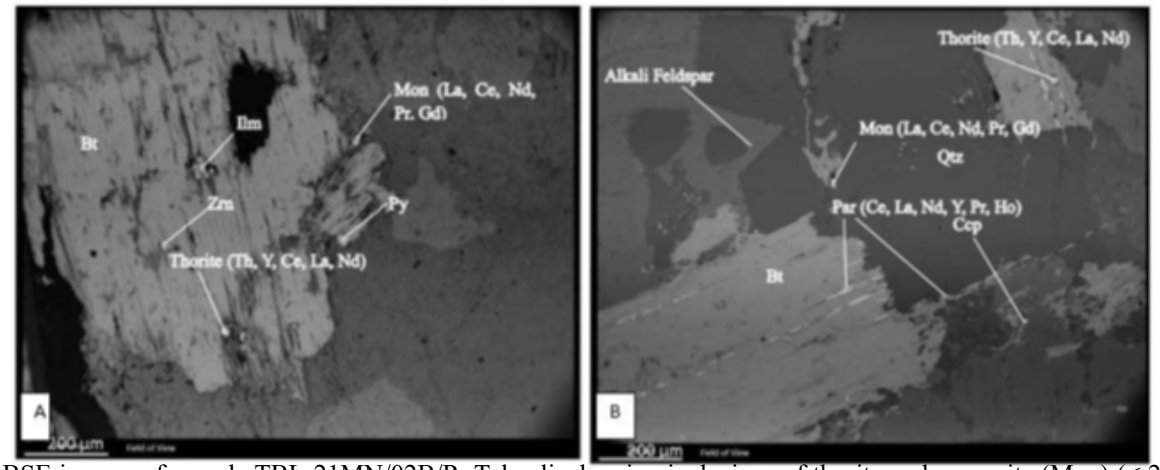

Figure 16: BSE images of sample TBL-21MN/02B/R, Toboali, showing inclusions of thorite and monazite (Mon) (< 2 µm) in biotite (A), Inclusions of monazite and thorite (< 2 µm) and biotite cleavage-filling parisite (B). In addition, chalcopyrite (Ccp) and ilmenite (Ilm) were seen in biotite

Monazite

The presence of the primary REE mineral in the form of monazite is shown from the results of EPMA, EDS, and BSE images analysis on a number of granite samples, especially from the Toboali. Monazites ranging in size from less than 10 µm to several tens µm are shown in the photomicrograph of the sample TBL-21MN/02B/R (Figures 9c, 9f, 13A, and 13B) as inclusions in biotite.

BSE image of granite sample hosting mineralized quartz veins TBL-21MN/14/R, Air Gegas (Figure 17) contains monazite inclusions filling cavities in rock-forming quartz [31-33]. The results of the analysis of the chemical composition of the EPMA method confirmed the presence of a significant amount of REE oxide compounds (Table 4). This REE compound is thought to have come from monazite.

Table 4: Chemical composition of EPMA at thorite spots of sample TBL-21MN/02B/R Toboali and TBL-21MN/05E/R Air Gegas

Chemical Compoun ds	TBL- 21MN/02B/R-Th-1	TBL- 21MN/02B/R-Th-2	21MN/05E/R Th-1
F	1.30	5.10	0.00
Al_2O_3	0.57	0.30	0.00
SiO2	14.61	2.59	7.38
P_2O_5	0.00	0.00	0.39
CaO	1.22	1.56	1.39
TiO_2	0.00	0.00	0.00
FeO	2.94	0.82	0.70
Y_2O_3	1.06	1.07	0.89
La_2O_3	0.03	0.11	0.40
Ce_2O_3	0.08	0.29	0.95
Pr_2O_3	0.00	0.00	0.06
Nd_2O_3	0.18	0.09	0.43
Gd_2O_3	0.15	0.13	0.33
Ho_2O_3	0.00	0.00	0.00
ThO_2	59.28	79.58	75.04
Total	81.403	91.631	87.964
Mineral	Thorite		Thorite

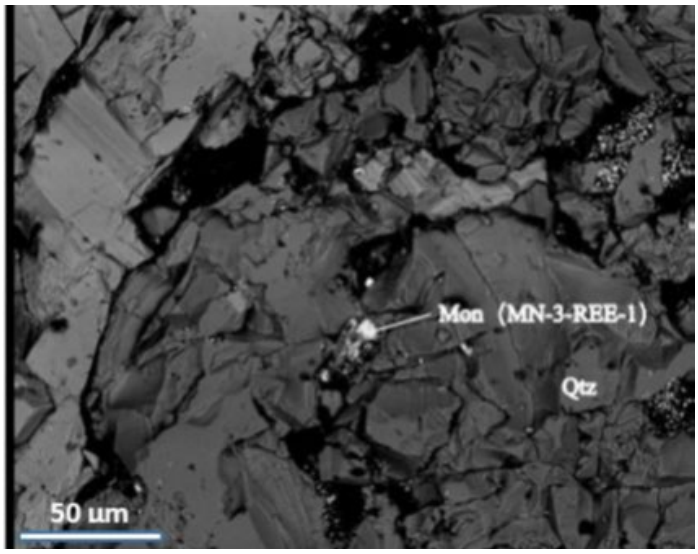

Figure 17: BSE image of sample TBL-21MN/14/R (spot MN-3-REE-1), Air Gegas, showing monazite inclusions in quartz. The REE oxide values from the EPMA analysis is shown in Table 3.

Bastnaesite

Based on the BSE images in Figure 11b, bastnaesite ((CeF) CO3) is present to fill cavities in plagioclase measuring 40 µm, indicating its formation after crystallization of granite sample TBL-21MN/02B/R, Toboali Region. Its formation was followed by parasite filling fractures in plagioclase. Bastnäsite, REECO3F, and synchysite, CaREE (CO3)2F, represent end members of a polysomatic mineral series including parasite, CaREE2(CO3)3F2, and röntgenite, Ca2REE3(CO3)5F3, as intermediate members [34].

Xenotime

Based on the BSE photomicrograph in Figure 11d, xenotime is present in the form of fine inclusions (< 2 µm) in biotite, indicating its formation as an REE mineral, especially Y along with magmatic crystallization of granite rock sample TBL-21MN/02B/R, Toboali. Its formation coincides with the deposition of other minerals such as zircon, sphalerite, and ilmenite in biotite.

Thorite

BSE images of sample TBL-21KP/07/F represent the radioactive mineral of thorite (Th,U SiO4) grains with 25 µm size, filling the cavity that cuts the biotite cleavage (Figure 13). This structure indicates that thorite was formed post-crystallization of granite. Thorite also appears as fine inclusions in the biotite granite sample TBL-21MN/02B/R (Figures 11c and 11f), indicating that its formation took place concurrently with biotite crystallization. Based on the EPMA analysis of samples TBL-21MN/02B/R and TBL-21MN/05E/R Confirmed that thorite also contains REE (Table 4).

Zircon

Under BSE images, zircon is the most common granite accessory found in rock samples. It is present in the form of inclusion grains (<2µm to 50µm) in biotite (Figures 11 and 18). Zircon is thought to form during the crystallization of rock-forming minerals such as biotite. In another site of this sample, zircon is present as fine inclusions in quartz along with fluorite and parasite (Figure 14c). In addition, zircon is also present together with other REE minerals in the BSE image of sample TBL 21KP-16/F (Figure 18).

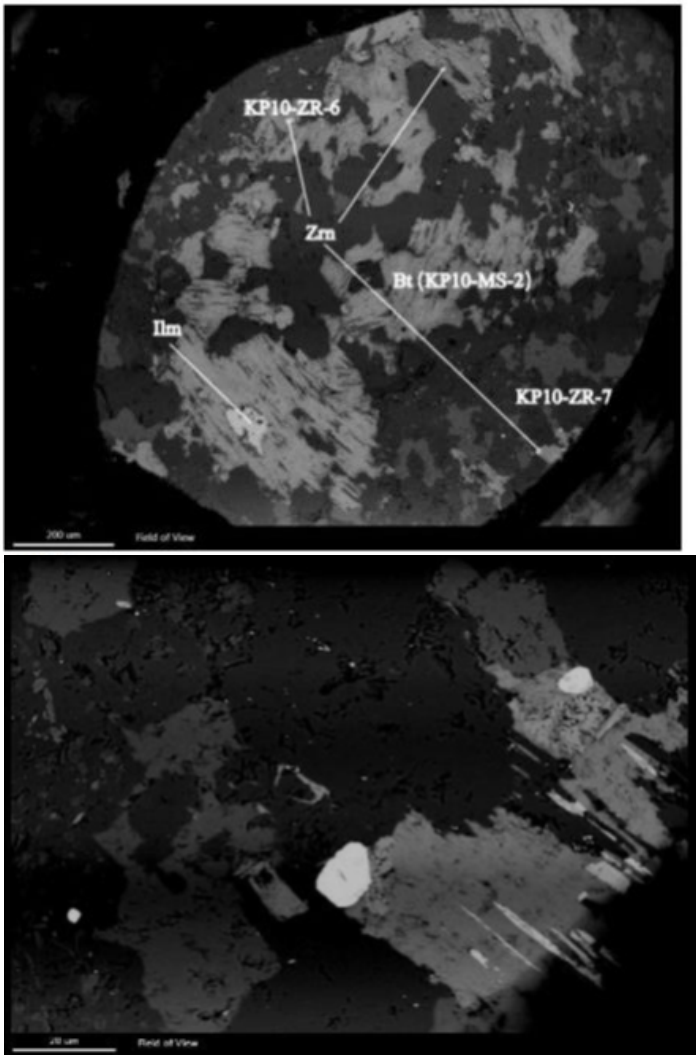

Figure 18: BSE images of sample TBL 21KP-16/F (laboratory code KP-10), Toboali, in the form of zircon inclusions (Zm) with the size from > 10 µm (left) until 10 or 20 µm (right)

REE content of zircon (Table 5) is represented by Y oxide compound with the range of 0.04 – 0.38 % determined using the EPMA analysis at the spot of the zircon surface. This zircon also contains Th ranging from 0.02 % to 0.33% analysed on the same spot.

Table 5: Chemical analysis of EPMA sample TBL 21KP-16/F (laboratory code KP-10)

Element	(KP10-ZR-4) TBL 21KP-16/F	(KP10-ZR-5) TBL 21KP-16/F	(KP10-ZR-6) TBL 21KP-16/F	(KP10-ZR-7) TBL 21KP-16/F
Al_2O_3	0.41	0	0.06	5.40
SiO_2	32.01	31.46	32.72	32.24
CaO	0.29	0.02	0.11	0.56
FeO	0.71	0.46	1.08	9.53
Y_2O_3	0.04	0.10	0.19	0.38
ZrO_2	62.52	64.10	64.87	44.19
HfO_2	1.25	1.50	1.54	1.96
ThO_2	0.33	0.02	0.04	0.23
Total	97.56	97.66	100.62	94.48

Fluid Inclusion

Based on observation of a sample quartz vein hosted in granitic rocks from Air Gegas (TBL-21MN/05E), quartz contains significant fluid inclusions that are well developed but small (Figure 19).

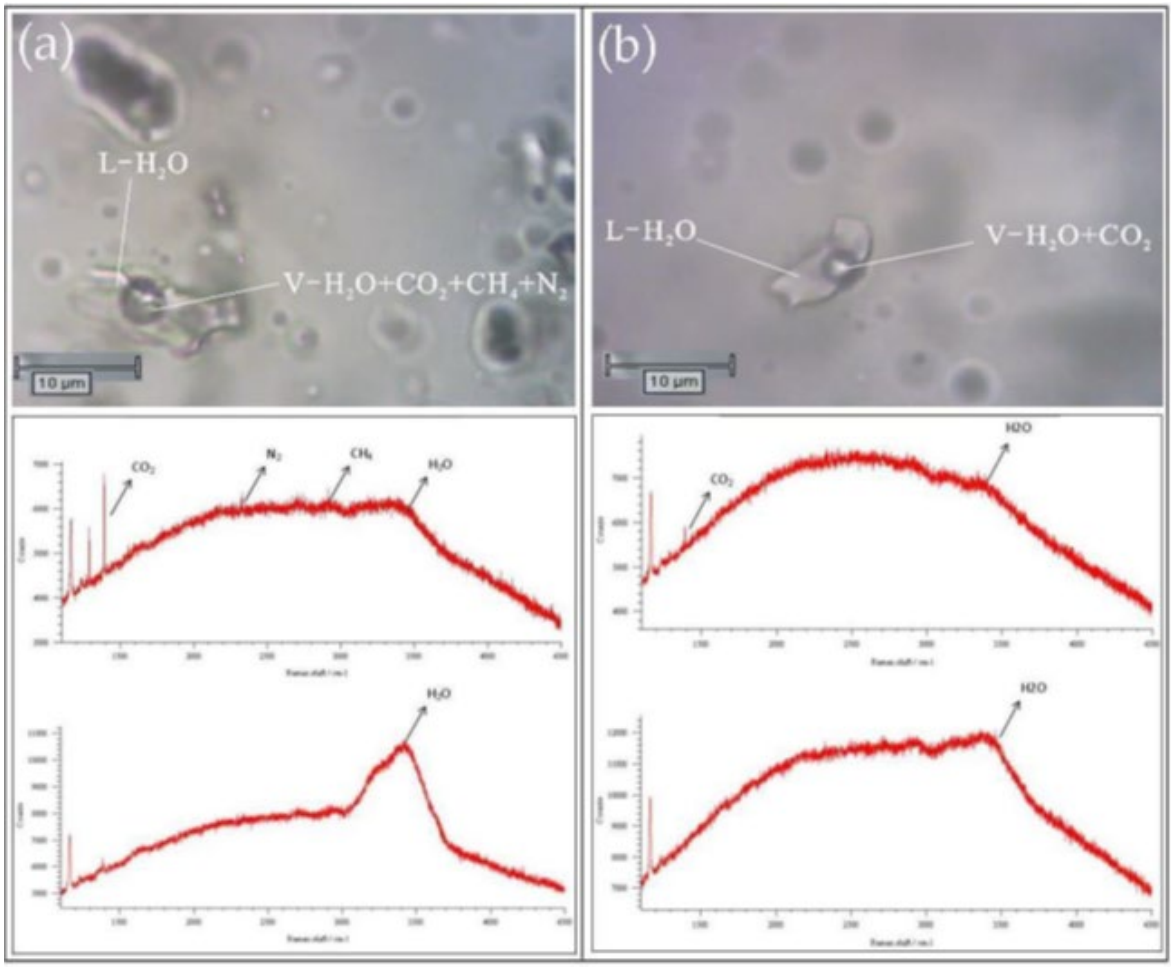

Figures 19: (a). Fluid inclusion type L+V (top photo) with the main components of H2O, CO2, CH4 and N2. Top curve, inclusion of type V fluid (vapour) with the main components H2O, CO2, CH4 and N2. The lower curve shows the Raman spectrum of the inclusion of an L-type fluid (liquid), with the main component of H2O. (b). Fluid inclusions of type L+V (top photo) with the main components H2O and CO2. Top curve, the inclusion of type V fluid (vapour), with CO2 and H2O components [35]. Bottom curve, Raman spectrum inclusions type L fluid (liquid), with the main component of H2O. Compositional analysis of L+V type inclusions in quartz by Laser Raman spectroscopy.

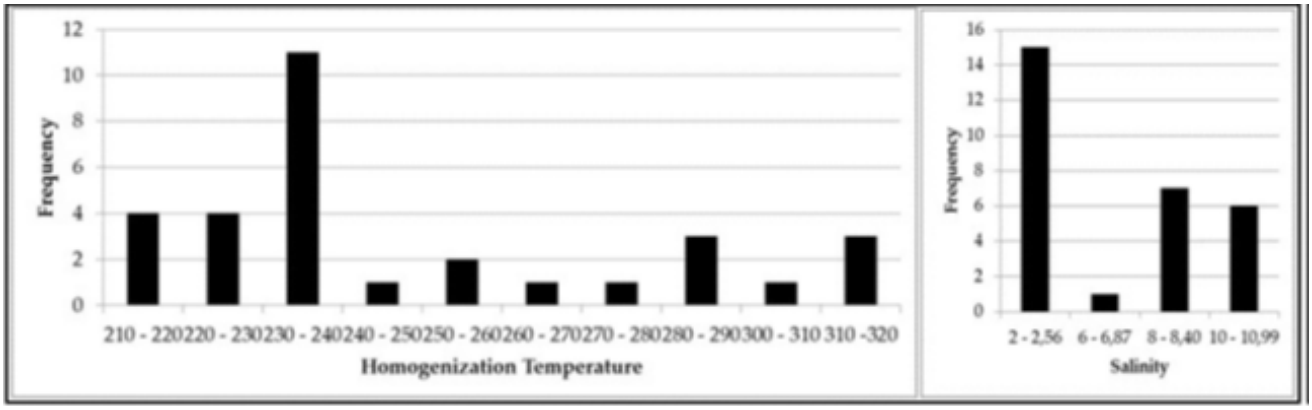

Figure 20: (a). Histogram of homogenization temperature. (b). Histogram of salinity

L+V type fluid inclusions (FIs)

• The L+V type FIs are widespread in quartz and are about 40% of the total FIs. The FIs exhibit long stripy, polygon, or irregular shapes, and their diameters range from 3 to 10 μm, individually 20μm. The FIs have VH2O/(VH2O+LH2O) = 20-30 vol%. The FIs are gathered in a small group. The final ice-melting temperature Tm is range from -1.3 to -7.4 , corresponding to Salinity from 2.23 to 10.99 wt.% NaCl and final homogenization temperature from 210 to 316 (Table 6). Histogram of homogenization temperature and

Salinity are shown in Figure 20.

• L type fluid inclusions (FIs): widespread and found in quartz, about 40% of the total FIs, exhibit ellipse, quadrilateral or irregular shapes, and their diameters range from 4 to 10 μm. A small group gathers the FIs.

• V type fluid inclusions (FIs): 20% of the total FIs, exhibit ellipse and nearly close circular, and their diameters range from 3 to 6 μm, gathered by a small group.

• L+V+S type fluid inclusions (FIs): the V type FIs are much less than other types. The FIs exhibit ellipse and polygon, and their diameters range from 3 to 8 μm. A small group gathers the FIs.

• LH2O+LCO2+VCO2 type fluid inclusions (FIs): the type FIs are much less than other types. The FIs exhibit ellipse and long stripy, and their diameters range from 8 to 12 μm. A small group gathers the FIs. The FIs have VCO2/(LH2O+LCO2+VCO2)=10-20 vol%, LCO2/(LH2O+LCO2+VCO2)=10-20 vol% and LH2O/(LH2O+LCO2+VCO2) = 6070 vol%. Its eutectic temperature is -76 , disappeared clathrate temperature +8.0 , partial homogenization temperature +26.8 , and final homogenization temperature 317 .Using equation wt.% NaCl = 15.52022 – 1.02342T – 0.95286T2 , T : final clathrate melting temperature (Htun et al., 2019), salinity were calculated to be 3.96 wt.%NaCl (Table 7).

Table 6: Homogenization Temperatures and Calculated Salinity Values

No	Final homogenization temperature (°C)	Ice-melting temperature (°C)	Final Salinity (wt % NaCl)	No	Final homogenization temperature (°C)	Ice-melting temperature (°C)	Final Salinity (wt % NaCl)
1	229	-7,4	10,99	16	212 (2)	-1,5	2,56
2	231	-7,4	10,99	17	223	-1,5	2,56
3	233	-7,4	10,99	18	210	-1,5	2,56
4	247	-7,4	10,99	19	261	-1,5	2,56
5	240	-7,4	10,99	20	253	-1,5	2,56
6	233	-7,4	10,99	21	251	-1,5	2,56
7	224	-1,3	2,23	22	312	-5,4	8,4
8	232	-1,3	2,23	23	311	-5,4	8,4
9	232	-1,3	2,23	24	277	-4,3	6,87
10	217	-1,3	2,23	25	286	-5,4	8,4
11	232 (2)	-1,3	2,23	26	310	-5,4	8,4
12	234	-1,3	2,23	27	289	-5,4	8,4
13	221	-1,3	2,23	28	281	-5,4	8,4
14	237	-1,3	2,23	29	316	-5,4	8,4
15	234	-1,3	2,23				

L=liquid; V=vapour; S=solid

Table 7: Data of Eutectic and Disappeared Clathrate Temperatures

Eutectic temperature (℃)	Disappeared clathrate temperature (℃)	Salinity(wt.%NaCl)	Partial homogenization temperature(℃)	Final Homogenization temperature (℃)
-76	+8.0	3.96	+26.8	317

Stable isotopes O and S

The results of stable isotope analysis of O and S for samples of mineralized quartz veins (TBL-21MN/05E and TBL-21MN/14/R) from Air Gegas are shown in Table 8. The analysed value of δ 34S from pyrite for the both samples is almost the same, namely 5.3 ‰ and 5.5 ‰, while the analysis results from sphalerite are only obtained from samples TBL-21MN/05E/R which is 3.9 ‰.

Table 8: Stable Isotope Values of Oxygen and Sulphur

Sample	Mineral	δ^{18}OV-PDB	δ^{18}OV-SMOW	δ^{34}SV-CDT/‰
TBL- 21MN/05E/R	Quartz	-17.3	13	-
	Pyrite	-	-	5.3
	Sphalerite	-	-	3.9
TBL-21MN/14/R	Quartz	-17.6	12.7	-
	Pyrite	-	-	5.5

The range of δ^{18}O values in quartz veins originating from magmatic fluids is generally 9,1 ‰ - 9,7 ‰. The value of oxygen stable isotopes in the study area is greater than this value range. In a large number of hydrothermal deposits, the value of δ18O ranging from 0‰ to 10‰ is interpreted as a result of mixing meteoric fluid with magmatic fluid. The stable isotope value of O in the study area is more positive, exceeding the range of magmatic fluids, possibly due to the effect of mixing water rather than the magmatic fluid.

The range of δ^{34}S values of sulphide from mineralized quartz veins of sample TBL-21MN/05E/R and TBL21MN/14/R, Air Gegas is from 3.9 ‰ to 5.5 ‰. This range lies in the typically range of granite rocks (-10‰ – 14‰), hydrothermal deposits (-30‰ - 22‰), hydrothermal vents (0 ‰– 5 ‰), and magnetite series granite (2 ‰ – 9 ‰) (Seal, 2006). In particular, the average sulphur isotope composition of pyrite (5.4 ‰) and sphalerite (3.9‰) for the quartz veins of TBL-21MN/05E/R and TBL-21MN/14/R were interpreted as originating from sedimentary rocks, metamorphic rocks and granitic rocks (Figure 22).

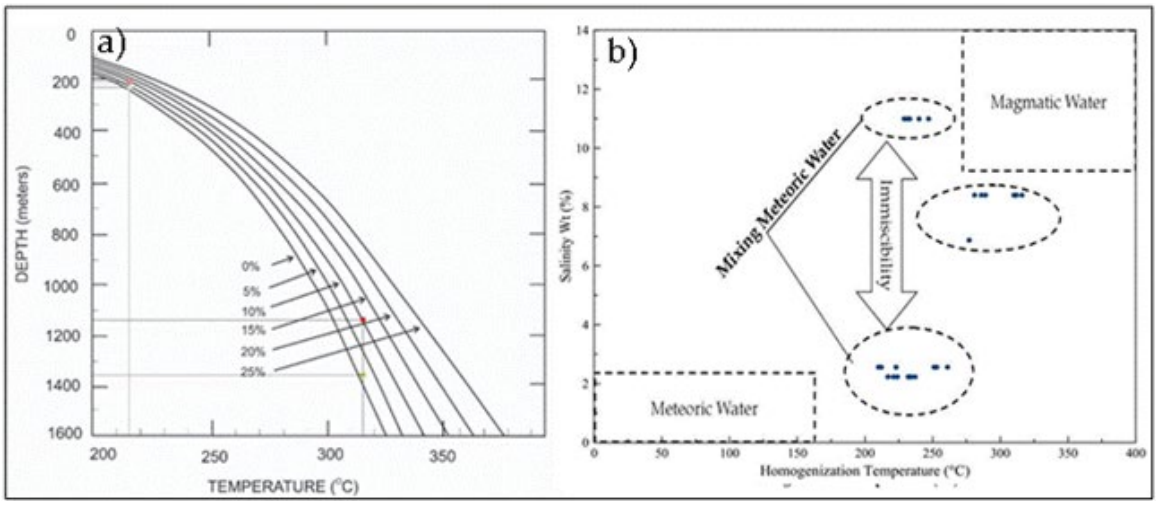

Figure 22: (a). Interpretation curve for mineralization depth in Air Gegas, South Bangka using the relation of homogenization temperature versus depth (Hass, 1971) (b) and fluid inclusion groups representing immiscibility and evolved mineralizing fluid

Discussion

REE-bearing granite characteristics

In general, the granites in the study area formed in a syn-collision tectonic environment, per aluminous in nature, with magma affinity of high K-calc alkaline series, and contain REE which range from 180.8 ppm to 1124.6 ppm. REE patterns of these samples show LREE enrichment as an indication of perfect fractionation. Two granite samples (TBL-21MN/02B/R and TBL-21KP/07/F) contain the highest REE up to 1124.6 ppm and 1014.69 ppm respectively with an LREE/HREE ratio of 7. The two granite samples show a positive anomaly in high field strength elements (HFSE) such as REE and radioactive elements while Zr, Nb, and P are depleted. The large ion lithophile elements (LILE) have negative anomalies, especially for Cs, Rb, K, and Ba (Figure 10b).

The highest REE content of two granitic rocks is thought to have resulted from the presence of primary REE minerals such as REE phosphate (monazite, xenotime, and apatite) and REE carbonate (parasite, allanite, and bastnaesite) as confirmed by BSE images. REE phosphate minerals are more dominant than carbonate ones. The distinguishing features of these two rocks included are a lesser negative anomaly of Eu compared to the other granite samples (Figure 10). It means that the two samples are fractionated less perfectly than the others (Figure 14). The presence of fine inclusions of fluorite along with parasite, and zircon in quartz of sample TBL-21MN/02B/R, Toboali, indicates that fluorite precipitated as a result of the changes in temperature and pressure along with the channel way of the hydrothermal solutions or due to fluid mixing or interactions with the wall rock [36]. It may be the result of the late crystallization of granite or magmatic fluid [37]. Since fluorite is spatially present together with inclusions of REE minerals such as parasite, and the considerable higher of LREE value than HREE, this may have resulted from precipitation in the early precipitated of fluorites, whereas HREE is enriched in late precipitated of fluorites [38]. It is suspected that this led to the enrichment of HREE especially Pr2O3 and Gd2O3 in the quartz vein in Air Gegas (TBL-21MN/05E/R) but depleted in the granite of Toboali (TBL-21MN/2B/R) as confirmed by EPMA analysis in Table 4. The presence of sulfide mineralization such as chalcopyrite and sphalerite in granite samples of TBL-21MN/02B/R (Figures 6 and 11) indicates that mineralizing fluid of post-magmatic crystallization may have affected this granite rock.

Characteristics and Composition of Hydrothermal Fluid

The significant REE content of up to 363.34 ppm (Table 1) in the sample TBL-21MN/05E/R, which is dominated by LREE with an LREE/HREE ratio of 10, is interpreted as originating from fracture-filling of parasites and fine inclusions of monazite in the quartz veins as confirmed by BSE images (Figure 12). Besides REE, this quartz vein sample also contains significant Sn, Cu, W, Pb, Zn, and Li values (Table 1), which is typically indicating a polymetallic tin deposit.

A quite large range of homogenization temperatures (210 – 316oC) and a wide range of salinity values (2.23 wt% NaCl – 10.99 wt% NaCl) indicate that there is more than one fluid phase in the sulphide-REE mineralization. The estimated depth of mineralization, based on the curve plot, range from 1150 m to 1350 m from the present surface (Figure 21 a). In accordance with homogenization temperatures, there are three different inclusion groups which represent the homogenization temperature interval between 212 oC and 261oC for the first group, 223 to 253 °C for the second group, and 277 to 316 °C for the third group (Figure 21b). In general, the temperature of the hydrothermal fluid in depositing cassiterite ranges from 250450oC. This shows that the temperature range for cassiterite formation in the Bangka Belitung Tin Belt is 210–450oC.

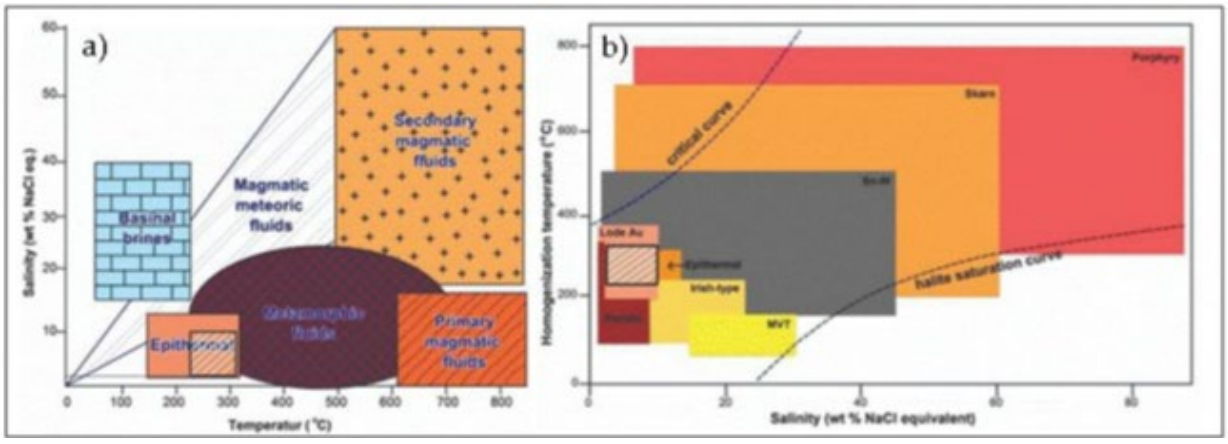

Figure 21: (a). Plot of fluid inclusions in the study area (shading) fall into the low temperature hydrothermal field that may come from metamorphic fluid (modified from Rajesh & Pankaj, 2014). (b). All fluid inclusion data are also within Au and Sn-W

Compared to the South Bangka which has a wide range of homogenization temperatures (210 – 316oC) indicates an evolving process of the hydrothermal solution system from high to low temperatures. On the other hand, there are no substantial differences in terms of the salinity of these two groups, ranging from 2.6 to 5.7 wt. % for the first group and 3.7 to 7.3 wt. % for the second group. These differences in homogenization temperatures may be caused by cooling towards the outer zones of quartz. Therefore, the first group is considered to be the early stage of mineralization according to the highest homogenization temperatures obtained from quartz (max 386.8 °C). Also, these differences may have resulted from a mixing of two different ore-forming fluids.

The inclusion type of fluid V (vapour) with the main components of H2O, CO2, CH4, and N2, and L (liquid) with the dominant component of H2O indicates that there is a separation process between fluid and vapor during hydrothermal activity or boiling at high homogenization temperatures, then decreases and releases CO2 (decarbonisation). The decrease in temperature is thought to be affected by an increase in the composition of the meteoric water upon mixing with the hydrothermal solution (Figure 21b). CO2 plays an important role in various types of ore deposits including REE, in relation to hydrothermal transport containing REE, therefore CO2 is an integral part of the ore mineralization system and has a partition level of REE [39]. From the spectrum of the Raman curve, it is reflected that the inclusions are dominated by CO2 gas components, while relatively few CH4 and N2 gases.

The results of the analysis of mineralized quartz veins hosted in granite (samples TBL-21MN/05E/R and TBL-21MN/14/R) Air Gegas show a range of 12,7 ‰ – 13 ‰ for δ18O, and 3,9 ‰ – 5,5 ‰ for δ34S. The value of the stable isotope of oxygen shows a small range, while the range of values of δ34S has a quite wide range. Referring to the relationship of salinity to homogenization temperature (Figure 22a and Figure 22b) it is interpreted that metamorphic water mixing is thought to affect the composition of δ18O hydrothermal fluid resulting in mineralization in the study area. This condition is supported by the local geology condition that the mineralized quartz veins (TBL-21MN/05E/R and TBL-21MN/14/R Air Gegas) analysed for fluid inclusions and stable isotopes are in contact with metamorphic rocks of the Pemali Complex (Figure 1). The range of $\delta^{34}S$ values is close to that of magmatic fluids, namely 0‰ – 5‰, similar with tin deposits in Brazilian Rondonia. However, in the context of the study area, the value of $\delta^{34}S$ is slightly more enriched, possibly influenced by an igneous sulphide reservoir that has a value range of -2 ‰ to + 35 ‰ [40]. Kelabat granite is the closest surrounding rock, it may be a stable isotope source of S for the sulphide mineralizing-hydrothermal fluid.

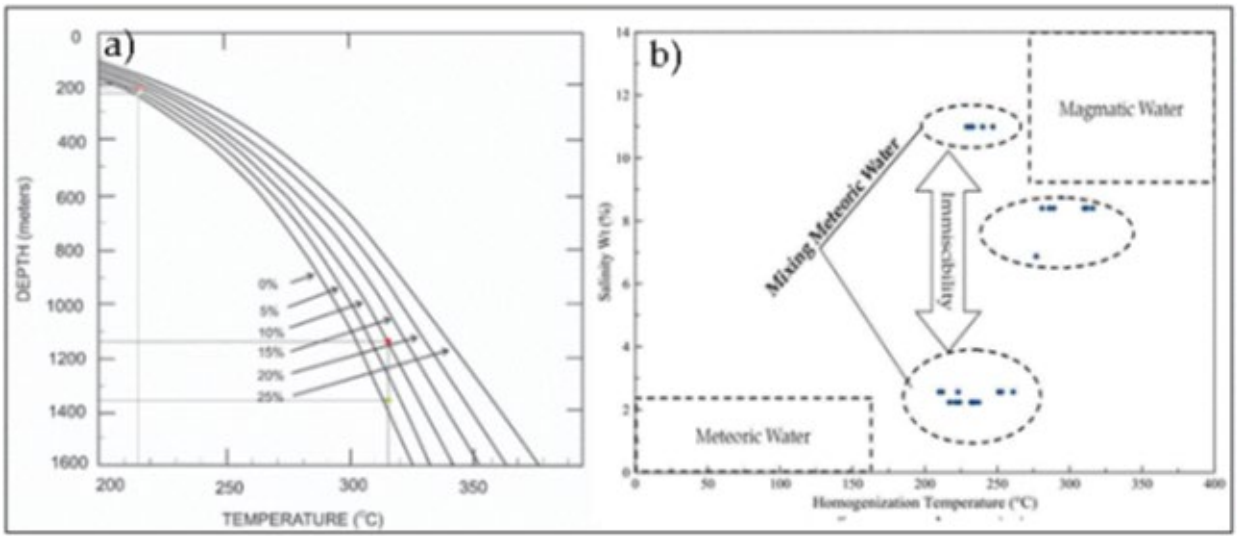

Figure 22: (a). Interpretation curve for mineralization depth in Air Gegas, South Bangka using the relation of homogenization temperature versus depth (Hass, 1971) (b) and fluid inclusion groups representing immiscibility and evolved mineralizing fluid

The presence of apatite in the quartz vein of sample TBL-21MN/05E/R (BSE images of Figure 15a and 15d) may have enriched REE. Apatite may substitute REEs during either formation or a later hydrothermal alteration, so that it is an indication of the role of late-stage hydrothermal and an indication of primary REE as a result of the heavy REE enrichment process.

Para genetic Sequence of Primary REE Minerals

Some indicators in estimating the stages of REE formation relative to other minerals are the presence of subhedral-euhedral crystals of REE minerals, the inclusion structure of REE minerals filling pores or between rock-forming minerals, fractures that provide space for REE mineral deposition, and fluorite. The shape of euhedral crystals in rock-forming minerals indicates that their formation coincided with early magma crystallization. REE min-

eral inclusions filling pores between rock-forming minerals are interpreted as REE precipitated at an intermediate stage. Fracture-infilling veins indicate that there is room for the circulation of mineralization-carrying solutions and their deposition, in the context of the studied area; it is interpreted as intermediate stages. The presence of quartz veins containing cassiterite and tourmaline mineralization is interpreted as the final stage of the hydrothermal solution.

From the results of fluid inclusion studies on quartz veins, which are in contact with the parent granitic rocks (sample TBL-21MN/05E/R), there are two types of fluid inclusions consisting of type V (vapour) with the main components H2O, CO2, CH4 dan N2, and type L (liquid or fluid) with the main component H2O (Figure 19). These data indicate that there is a separation process between fluid and gas during hydrothermal activity or boiling (Shepherd et al., 1985). This corresponds to the composition of the vapour inclusions. The temperature of mineralization formation associated with hydrothermal fluid can be interpreted from the homogenization temperature data. Referring to the histogram in Figure 20, the temperature of the formation of tin mineralization and REE minerals (parasites, monazite, and zircon) is estimated to be in the range of 210 – 316o C.

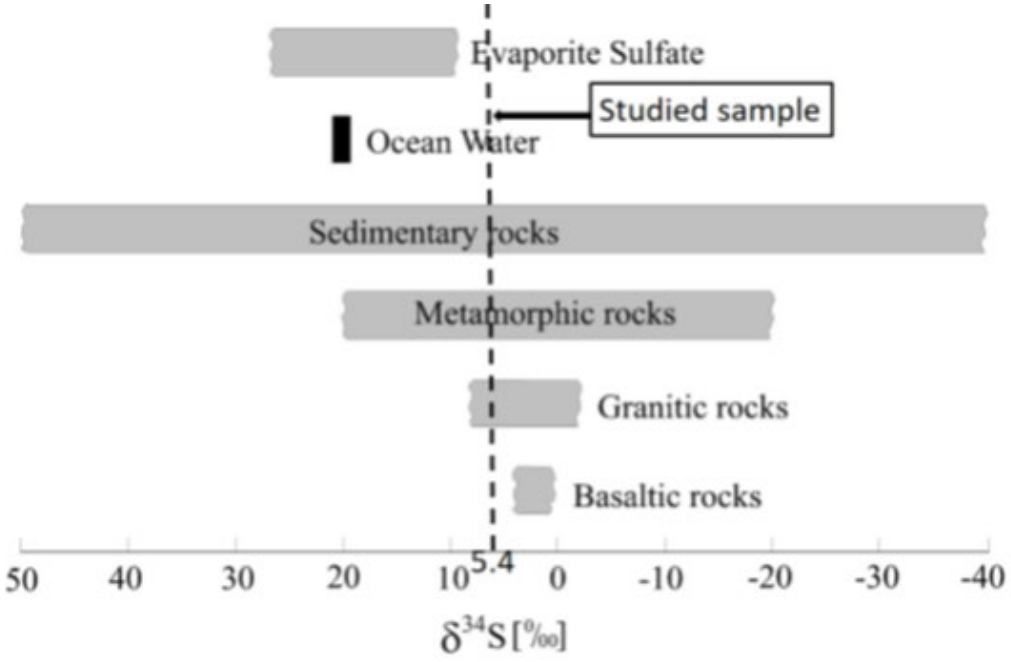

Figure 23: Sulphur isotope composition of sphalerite and pyrite of samples from Air Gegas

A plot of the salinity vs temperature homogenization (Figure 20) shows that the curve partially overlaps with the metamorphic fluid region. Referring to field data, the sample (TBL-21MN/05E/R) is located at the contact between metamorphic rocks (phyllite, schist, and quartzite) of the Pemali Complex and Kelabat Granite (Figure 1). Hence, the composition of the hydrothermal solution may be influenced by the metamorphic solution.

Referring to the homogenization temperature range and salinity, there are three mineralization phases. The initial phase is magmatic crystallization, which produces a magmatic-hydrothermal solution with an estimated temperature range of > 316 oC - 316oC. At this early stage, pyrite is formed along with a small amount of chalcopyrite and REE minerals (monazite and xenotime). In the second stage which is magmatic hydrothermal, it is estimated that at a temperature range of < 316oC - 210 oC metallic sulfide and REE minerals (monazite, parasite, bastnaesite, and allanite) are formed. In the third stage, the temperature of formation of sulfide minerals (pyrite-py, sphalerite-sf) within the mineralized quartz veins (TBL-21MN/05E/R Air Gegas) can be estimated using the formula: T = (0,55 ± 0,04) x 103)/(Δpy-sf)½ - 273 oC atau Δpy-sf = 0,30 x 106 / T2 - 273 oC (Ohmoto & Rye, 1970; Seal, 2006). From the calculation, temperature (T) value is 190 oC In terms of mineral par agenesis in the study area, sulfide minerals are formed up to the final stage of the hydrothermal solution with the temperature range of < 210 oC – 190 oC, by which pyrite, sphalerite, monazite, parasite, and bastnaesite are formed. Hence, the sequence of mineral par agenesis can be arranged as shown in Figure 24.

Minerals	Early stage magmatic crystallization (≥ 316°C)	Medium stage (magmatic hydrothermal) (< 316°C–210°C)	Late stage hydrotermal (< 210°C–190°C)
Biotite	==========		
Alkaline feldspar	.....		
Plagioclase	=======		
Quartz	=======	=========	==========
Muscovite	.....		
Fluorite		.....	
Apatite		.....	
Zircon	=======		
Ilmenite	———		
Rutile			.....
Cassiterite		.....	==========
Stannite		———	
REE-Bearing Minerals :			
- Monazite	==========	=========	———
- Xenotime	———		
- Parisite		==========	
- Allanite		==========	———
- Bastnasite		———	.....
- Zircon	———		
- Thorite		.....	
Metallic sulfide :			
- Chalcopyrite	.....	.....	
- Sphalerite		———	———
- Pyrite	———	==========	———

==== :Abundant; ——— : Common; ..... : Minor

Figure 24: Para genetic Mineral Sequences

Conclusion

Primary REE mineral types, which are the main source of REE in South Bangka, can be divided into three groups, namely REE phosphate consisting of monazite, xenotime, and apatite, REE carbonate consisting of parasite, allanite, and bastnaesite, and other REE-bearing radioactive minerals such as thorite and zircon inclusions. The REE phosphate mineral group is hosted in granite, which is formed in the early magmatic crystallization and magmatic-hydrothermal stages. While monazite seems to have formed in quartz veins together with cassiterite. The main granite host rocks are per aluminous and S-type.

The carbonate REE group is thought to have formed from the intermediate magmatic-hydrothermal to the late hydrothermal stage. Cassiterite, stannite, chalcopyrite, and sphalerite are interpreted to form at the same stage as REE. However, the highest total REE

values were found in the Toboali mineralized granite parent rock, but not in the granite as a host of mineralized quartz veins. Research on REE deposits within hydrothermal solutions is an interesting program for finding primary REE deposits of economic value in the future. However, REE with granite has more potential for weathering products, in both alluvial and weathering deposits.

The sulphur isotope composition is thought to originate from granite rocks, which are part of the Klabat Granite emplacement. While the oxygen isotope composition is a meteoric mixture but it seems also to have been influenced by metamorphic fluids. This is thought to be related to the metamorphic rocks of the Pemali Metamorphic Complex. Research on the existence of this metamorphic rock and its effect on REE deposition is necessary to follow up in the future.

Acknowledgments

Authors express great knowledge to the Director-General of Mineral and Coal of Indonesia for funding REE inventory project 2021 and the head of the Centre for Mining Technology Development. The authors also appreciate the head of the Centre for Mineral Coal and Geothermal Resources appointing Armin Tampubolon as team coordinator and allow using data analyses. Last, the authors also acknowledged the local porters who have assisted during fieldwork.

Data Availability Statement

Not applicable

References

1. Weng, Z., Mudd, G. M., Jowitt, S. M., & Haque, N. (2017). Assessment of global rare earth supply and wind energy growth: opportunities and challenges. In 2nd Green and Sustainable Chemistry conference.
2. Wang, Z. Y., Fan, H. R., Zhou, L., Yang, K. F., & She, H. D. (2020). Carbonatite-related REE deposits: An overview. Minerals, 10(11), 965.
3. Soetopo, B. (2013). Studi Geologi dan Logam Tanah Jarang (RE) Daerah Air Gegas, Bangka Selatan. Eksplorium, 34(1), 51-62.
4. Tampubolon, A., Muhammad A. & Prima H.M. (2015). Rare Earth Elements, Indonesian Minerals Year Book, Centre for Mineral Coal and Geothermal Resources, p.95-104.
5. Zglinicki, K., Szamałek, K., & Wołkowicz, S. (2021). Critical minerals from post-processing tailing. A case study from Bangka Island, Indonesia. Minerals, 11(4), 352.
6. Harlov, D. E. (2015). Apatite: A fingerprint for metasomatic processes. Elements, 11(3), 171-176.
7. Hamdan, Z.A., Baharuddin & Surawardi in Metallogeni Sundaland Vol I (Ed.). (2014). Toboali Alluvial Tin Deposit: Geology, depositional processes, and material sources. Badan Geologi.137-150.
8. SITHA, K. (2009). Characteristics of granitic rocks of Bangka Island, Indonesia, and their associated mineralization (Doctoral dissertation, Universitas Gadjah Mada).
9. Ng, S. W. P., Whitehouse, M. J., Roselee, M. H., Teschner, C., Murtadha, S., Oliver, G. J., & Chang, S. C. (2017). Late triassic granites from Bangka, Indonesia: A continuation of the main range granite province of the South-East Asian tin belt. Journal of Asian Earth Sciences, 138, 548-561.
10. Mangga, S.A., & Djamal, B. (1994). Geologic Map of North Bangka Quadrangle, Scale 1: 250,000. Geological Research and Development Centre.
11. Margono, U., Supandjonom, E. & Partoyo, E., (1995). Geologic Map of South Bangka Quadrangle, Scale 1: 250,000. Bandung. Geological Research and Development Centre.
12. Hutchison, C. S. (2014). Tectonic evolution of Southeast Asia. Bulletin of the Geological Society of Malaysia, 60.
13. Schwartz, M. O., Rajah, S. S., Askury, A. K., Putthapiban, P., & Djaswadi, S. (1995). The southeast Asian tin belt. Earth-Science Reviews, 38(2-4), 95-293.
14. Crow, M. J., & Van Leeuwen, T. M. (2005). Chapter 12 Metallic mineral deposits. Geological Society, London, Memoirs, 31(1), 147-174.
15. Hamdan, Z.A., Baharuddin & Surawardi in Metallogeni Sundaland Vol I (Ed.). (1999). Toboali Alluvial Tin Deposit: Geology, depositional processes, and material sources. Indonesia Mining Journal.1-12.
16. Nascimento, T. M. F. D., & Souza, V. D. S. (2017). Mineralogy, stable isotopes (δ18O and δ34S) and 40Ar-39Ar geochronology studies on the hydrothermal carapace of the Igarapé Manteiga W-Sn Deposit, Rondônia. Brazilian Journal of Geology, 47, 591-613.
17. Möller, P., Parekh, P. P., & Schneider, H. J. (1976). The application of Tb/Ca-Tb/La abundance ratios to problems of fluorspar genesis. Mineralium Deposita, 11(1), 111-116.
18. Randive, K. R., Hari, K. R., Dora, M. L., Malpe, D. B., & Bhondwe, A. A. (2014). Study of fluid inclusions: methods, techniques and applications. Geol. Mag, 29, 19-28.
19. Shu, X., Liu, Y., & Li, D. (2020). Fluid inclusions as an indicator for REE mineralization in the Lizhuang deposit, Sichuan Province, Southwest China. Journal of Geochemical Exploration, 213, 106518.
20. Ohmoto, H. & Rye, R.O. (1970). Isotopes of sulfur and carbon: In Barnes, H.L. (ed.). Geochemistry of hydrothermal ore deposit. Second Ed. New York. Wiley 509-567.
21. Jia, Y. H., & Liu, Y. (2020). REE enrichment during magmatic–hydrothermal processes in carbonatite-related REE deposits: a case study of the weishan REE deposit, China. Minerals, 10(1), 25.
22. Shepherd, T.J., Rankin, A.H., Alderton, D.M.H., (1985). a practical guide to fluid inclusion studies. Glasgow: Blackie; New York: Distributed in the USA by Chapman and Hall.
23. Mirza, T. A., & Rashid, S. G. (2018). Mineralogy, Fluid inclusions and stable isotopes study constraints on genesis of sulfide ore mineral, Qaladiza area Qandil Series, Iraqi Kurdistan Region. Arabian Journal of Geosciences, 11(7), 1-15.
24. Owens, C. L., Nash, G. R., Hadler, K., Fitzpatrick, R. S., An-

derson, C. G., & Wall, F. (2019). Apatite enrichment by rare earth elements: A review of the effects of surface properties. Advances in colloid and interface science, 265, 14-28.
25. Deer, W. A. (2013). An introduction to the rock-forming minerals. London: The Mineralogical Society. ISBN 9780-903056-27-4. OCLC 858884283.
26. Prihutama, F. A., Syarifuddin, M., Ryandhika, A. I. A. F., Yogatama, S. A. W., & Aviandono, R. (2019, November). Structure System and It Controls to Mineralization of Primary Tin Deposit, Airdibi Area, Jebus Subdistrict, West Bangka, Bangka and Belitung. In Journal of Physics: Conference Series (Vol. 1363, No. 1, p. 012029). IOP Publishing.
27. Haas, J. L. (1971). The effect of salinity on the maximum thermal gradient of a hydrothermal system at hydrostatic pressure. Economic geology, 66(6), 940-946.
28. Htun, K. T., Yonezu, K., Myint, A. Z., Tindell, T., & Watanabe, K. (2019). Petrogenesis, ore mineralogy, and fluid inclusion studies of the Tagu Sn–W deposit, Myeik, Southern Myanmar. Minerals, 9(11), 654.
29. Widana, K. S. (2013). Petrografi dan Geokimia Unsur Utama Granitoid Pulau Bangka: Kajian Awal Tektonomagmatisme. Eksplorium, 34(2), 75-88.
30. McDonough, W.F. & Sun, S.S. (1989). Chemical and isotopic systematics of oceanic basalts Implications for mantle composition and processes. Geol. Soc. Lond. Spec. Publ., 42, 313–345.
31. McDonough, W. F., & Sun, S. S. (1995). The composition of the Earth. Chemical geology, 120(3-4), 223-253.
32. Middlemost, E. A. (1994). Naming materials in the magma/igneous rock system. Earth-science reviews, 37(3-4), 215-224.
33. Pearce, J. A., Harris, N. B., & Tindle, A. G. (1984). Trace element discrimination diagrams for the tectonic interpretation of granitic rocks. Journal of petrology, 25(4), 956-983.
34. Peccerillo, A., & Taylor, S. R. (1976). Geochemistry of Eocene calc-alkaline volcanic rocks from the Kastamonu area, northern Turkey. Contributions to mineralogy and petrology, 58(1), 63-81.
35. Verplanck, P. L. (2017). The role of fluids in the formation of rare earth element deposits. Procedia Earth and Planetary Science, 17, 758-761.
36. Sharma, R., & Srivastava, P. K. (2014). Hydrothermal fluids of magmatic origin. In Modelling of magmatic and allied processes (pp. 181-208). Springer, Cham.
37. Richardson, C. K., & Holland, H. D. (1979). Fluorite deposition in hydrothermal systems. Geochimica et Cosmochimica Acta, 43(8), 1327-1335.
38. Seal, R. R. (2006). Sulfur isotope geochemistry of sulfide minerals. Reviews in mineralogy and geochemistry, 61(1), 633-677.
39. Shand, S.J., (1943). Eruptive Rocks. Their Genesis Composition. Classification and Their Relation to Ore-Deposits with a Chapter on Meteorite. John Wiley & Sons, New York.
40. Zeug, M., Nasdala, L., Ende, M., Habler, G., Hauzenberger, C., Chanmuang N, C., & Wirth, R. (2021). The parisite–(Ce) enigma: challenges in the identification of fluorcarbonate minerals. Mineralogy and petrology, 115(1), 1-19.